

This manuscript has been authored by UT-Battelle, LLC under Contract No. DE-AC05-000R22725 with the U.S. Department of Energy. The United States Government retains and the publisher, by accepting the article for publication, acknowledges that the United States Government retains a non-exclusive, paid-up, irrevocable, world-wide license to publish or reproduce the published form of this manuscript, or allow others to do so, for United States Government purposes. The Department of Energy will provide public access to these results of federally sponsored research in accordance with the DOE Public Access Plan (http://energy.gov/downloads/doe-public-access-plan).



1	Ti	tle: Temperature Dependence of Elastic and Plastic Deformation Behavior
2		of a Ductile Refractory High-entropy Alloy
3	Au	thors: Chanho Lee ¹ , George Kim ² , Yi Chou ³ , Brianna L. Musicó ¹ , Michael C. Gao ⁴ , Ke An ⁵ ,
4		Gian Song ⁶ , Yi-Chia Chou ³ , Veerle Keppens ¹ , Wei Chen ² , and Peter K. Liaw ^{1*}
5	Affi	liations:
6	1	Department of Materials Science and Engineering, The University of Tennessee,
7		Knoxville, TN 37996-2100, USA
8	2	Department of Mechanical, Materials, and Aerospace Engineering, Illinois Institute of
9		Technology, Chicago, IL 60616, USA
10	3	Department of Electrophysics, National Chiao Tung University, Hsinchu, 30010, Taiwan
11	4	National Energy Technology Laboratory/Leidos Research Support Team, Albany, OR
12		97321, USA
13	5	Neutron Scattering Division, Oak Ridge National Laboratory, Oak Ridge, TN 37831,
14		USA
15	6	Division of Advanced Materials Engineering, Kongju National University, Cheonan,
16		Chungnam, 330-717, Republic of Korea
17		
18		
19		
20	*Co	rresponding author.



1	Email address: pliaw@utk.edu
2	Phone number: +1-865-974-6356
3	One Sentence Summary
4	The unique elastic and plastic deformation behaviors of the single BCC solid-solution
5	phase refractory HEA at elevated temperatures have been comprehensively studied, using in-situ
6	neutron experiments coupled with theoretical calculations.
7	
8	
9	
10	
11	
12	
13	
14	
15	
16	
17	
18	
19	
20	
21	
22	
23	



3

4

5

6

7

8

9

10

11

12

13

14

15

16

17

18

Abstract

Single-phase solid-solution refractory high-entropy-alloys (HEAs) show remarkable mechanical properties, such as high yield strengths with significant softening resistance at elevated temperatures. Hence, the in-depth study of the deformation behavior for body-centeredcubic (BCC) refractory HEAs is a critical issue to explore the uncovered/unique deformation mechanisms. We have investigated the elastic- and plastic-deformation behaviors of a single BCC NbTaTiV refractory HEA at elevated temperatures, using integrated experimental efforts and theoretical calculations. The in-situ neutron-diffraction results reveal a temperaturedependent elastic anisotropic-deformation behavior at elevated temperatures. The single-crystal elastic-moduli and macroscopic Young's, shear, and bulk moduli were determined from the insitu neutron diffraction, showing great agreement with first-principles calculations, machinelearning, and resonant-ultrasound-spectroscopy results. Furthermore, the edge-dislocationdominant plastic-deformation behaviors, which are different from conventional BCC alloys, were quantitatively described by the Williamson-Hall plot profile modeling, which is further experimentally verified by the high-angle-annular-dark-field (HAADF) scanning-transmissionelectron-microscopy (STEM).

19

20

21

22



Main Text

INTRODUCTION

High-entropy alloys (HEAs) are defined as equimolar or non-equimolar single-phase and multi-phase solid solutions, depending on the number and type of principal/secondary metallic elements with the configurational entropy greater than 1.61R, (where R is gas constant) (1, 2). The minimization of the Gibbs free energy by increasing the configurational entropy results in the formation of a single or multi-phase solid solution, such as body-centered-cubic (BCC) (3), face-centered-cubic (FCC) (4), and/or hexagonal-close-packed (HCP) solid-solution phases (5) instead of intermetallic compounds (6). Moreover, the random distribution of multiple elements with different atomic radii leads to a severely-distorted lattice with variation in the interatomic distances along the crystallographic direction of the unit cells (3, 7). These features, in turn, contribute to desirable mechanical properties, such as high hardness, strength, ductility, and softening resistance at room and elevated temperatures (3).

To identify the origin of these desirable mechanical properties, theoretical efforts have been conducted to verify the deformation mechanisms, by considering the elastic and plastic deformations in the BCC refractory HEAs (8). In contrast to conventional BCC alloys that have a narrow distribution of interatomic distances, HEAs possess a wider variety of bond lengths and atomic interactions in the unit cell, which may play a role in the unique elastic- and plastic-deformation behaviors at room and high temperatures.

Recently, Tian *et al.* (8) suggested alloy-design strategies to develop elastically-isotropic HEAs (TiZrNbMoV_x systems), using state-of-the-art ab-initio simulations. According to their



calculations, the TiZrNbMo_yV_x [where (x, y) are (0, 0.9) and (0.5, 0.8)] refractory HEAs exhibit the elastically-isotropic deformation behavior, which is strongly correlated to the value of the valence electron concentration (VEC) (8). Furthermore, these previous investigations provide criteria to evaluate the brittle-ductile behaviors based on single-crystal elastic constants, predicting that a few BCC HEA systems can be ductile (8-10). However, the validity of these theoretical calculation methods to design the elastically-isotropic and ductile BCC HEAs are still under debate and are lacking experimental validation (8, 11), which are critical issues within the HEA community.

To demonstrate these predicted unusual deformation behaviors, we investigated the elastic- and plastic-deformation behavior for the NbTaTiV BCC refractory HEA at room and elevated temperatures, using in-situ neutron experiments as well as theoretical approaches. Different from the conventional BCC alloys (12), the lattice-strain evolution and measured diffraction elastic moduli indicate the elastically-isotropic behavior at room temperature. The magnitude of single-crystal and macroscopic elastic moduli, obtained by in-situ neutron experiments and resonant ultrasound spectroscopy (RUS), respectively, are compared to theoretical calculations, including first-principles calculations and machine-learning (ML) approaches. Furthermore, it is found that the temperature-dependent elastic anisotropic-deformation behavior occurs at high temperatures, which is typically observed in conventional alloys (12, 13).

The excellent plasticity of the present refractory HEA can be predicted by the relationship between the polycrystalline elastic moduli, such as the Cauchy pressure $(C_{12}-C_{44})$ (14), Pugh ratio [bulk modulus (K) / shear modulus (G)] (9), and Poisson's ratio (v) (10). Moreover, we investigated the type of mobile dislocations, using the neutron-diffraction peak-



broadening modeling and analysis employing the Williamson-Hall plot method (15), experimentally verified by the high-angle-annular-dark-field (HAADF) scanning-transmission-electron-microscopy (STEM) technique. It is found that the dominant type of mobile dislocations during plastic deformation could be edge dislocations, which is different from conventional BCC metals. These new discoveries of unique elastic and plastic deformation behaviors in the NbTaTiV refractory HEA will facilitate the development of possible alloy systems for structural-material applications.

RESULTS

Formation of the single BCC solid solution and the mechanical properties of the homogenization-treated NbTaTiV HEA at elevated temperatures

The microstructure of the homogenized NbTaTiV refractory HEA was characterized, using the scanning-electron microscopy (SEM) back-scattered electrons (BSE) technique, as shown in Fig. 1A. A typical simple solid-solution HEA microstructure with grain sizes of 200 – 400 μm was identified without the presence of secondary phases or elemental segregations. The chemical composition of the sample was verified (using the point energy-dispersive X-ray spectroscopy analysis) to be Nb_{23.8}Ta_{25.5}Ti_{24.9}V_{25.8}, indicating a homogeneous elemental distribution in a nearly-equi-atomic percentage. The measured neutron diffraction (ND) patterns of the bulk samples, as illustrated in Fig. 1B, confirm the single BCC solid solution at room as well as elevated temperatures. The lattice parameters of the present alloy at room temperature (RT), 500 °C, 700 °C, and 900 °C, which were determined by a single-peak fitting approach (16), are 3.2318, 3.2445, 3.2511, and 3.2588 Å, respectively. The single BCC phase is stable up to 900 °C, indicating the excellent phase stability at elevated temperatures. Figure 1C shows the nominal compressive true stress-strain curves, as obtained from the in-situ neutron measurement



of the homogenization-treated NbTaTiV alloy at RT, 500 °C, 700 °C, and 900 °C with an estimated-strain rate of 1×10^{-4} s⁻¹, which were directly obtained from the in-situ neutron measurement. The yield strength (σ_y) and work-hardening exponent (N) of the present alloy gradually decreased from 1,064 MPa (RT) to 595 MPa (900 °C) and from 0.2732 (RT) to 0.1199 (900 °C), respectively. The work-hardening exponent (N) was estimated for the different experimental temperatures, using the Holloman equation (17):

$$\sigma_{t} = k \, \varepsilon_{t}^{N} \tag{1}$$

where σ_t is the true applied stress, k is the strengthening coefficient, and ε_t is the true plastic strain. During plastic deformation, the applied load relaxes slightly, while the neutron-recording time was set to approximately 20 minutes, with a constant displacement-control mode at 700 °C. Moreover, this relaxation behavior becomes more pronounced at 900 °C (about 440 – 580 MPa), as compared to 700°C (about 130 – 260 MPa), presented in Fig. 1C.

Lattice-strain evolutions of the homogenized NbTaTiV alloy at room and elevated temperatures

In-situ ND with compression tests on the homogenization-treated NbTaTiV alloy were carried out to investigate the elastic-deformation behavior for grains with different orientations. Figure 2 shows the corresponding lattice-strain (ε_{hkl}) evolution along the axial and transverse directions of the {110}, {200}, {211}, and {310} planes, during elastic deformation at various temperatures (RT, 500 °C, 700 °C, and 900 °C). The lattice strains were obtained from the following equation:

$$\varepsilon_{hkl} = \frac{d_{hkl} - d_{hkl}^{i}}{d_{hkl}^{i}} \tag{2}$$



where d_{hkl} is the hkl lattice spacing of the corresponding applied stress, and d_{hkl}^i is the hkl lattice spacing before loading. The slope of the lattice-strain evolution versus applied stress, during elastic deformation, determines the diffraction elastic constants for the specific $\{hkl\}$ oriented-planes. It was found that the variation in diffraction elastic constants among all the oriented grains is not clearly observed, indicating the elastically-isotropic deformation behavior, as presented in Fig. 2A.

Unlike the lattice-strain evolution at RT, different slopes in the lattice strains versus applied stresses at elevated temperatures are observed due to the increased elastic anisotropy, as presented in Figs. 2B to D. At higher temperatures, where the overall stiffness is reduced, the anisotropy increases. The $\{200\}$ -oriented grain exhibits the largest elastic lattice strain with the lowest stiffness, and the $\{310\}$ grains undergo the second largest elastic strain with a nearly-linear response. Whereas the $\{110\}$ and $\{211\}$ grains present lower lattice strains and higher directional strength-to-stiffness ratios than other orientations, the diffraction elastic moduli, E_{hkl} , of different crystallographic planes at elevated temperatures (listed in the Supplementary Table S1) shows almost the same values of elastic moduli in different orientations. This trend indicates that the NbTaTiV HEA exhibits the unique elastic-isotropic-deformation behavior at RT. Furthermore, the elastic anisotropy was gradually increased at elevated temperatures, which is the typical elastic-deformation behavior of conventional BCC structure alloys at RT (12, 13, 18). Calculations and measurements of single-crystal elastic moduli for the NbTaTiV alloy via the Kroner model and resonant-ultrasound-spectroscopy (RUS) technique

In order to better understand the underlying elastic-deformation behavior of the NbTaTiV alloy, as a function of temperature, the macroscopic elastic, shear, and bulk moduli (E_M , G_M , and K_M) are obtained from the diffraction elastic moduli (E_{hkl}) and Poisson's ratio (ν), by applying



2

3

4

5

6

7

8

9

10

11

12

13

14

15

16

17

18

19

20

21

22

theoretical models. The three most-widely applied theoretical models to determine the macroscopic elastic moduli are the Voigt, Reuss, and Kroner models, respectively (19, 20).

Figures 2E to H show the reciprocal diffraction elastic moduli $(1/E_{hkl})$ and v_{hkl}/E_{hkl} as a

function of the elastic-anisotropy factor, A_{hkl} , $\left[\frac{h^2k^2+k^2l^2+l^2h^2}{\left(h^2+k^2+l^2\right)^2}\right]$, which are obtained from the experimental elastic-lattice strain and calculated by the Voigt, Reuss, and Kroner models at room and elevated temperatures (19, 20). The results, as exhibited in Figs. 2E to H, indicate that the Kroner model is in the best agreement with the experimental data for all temperature ranges, as compared to the Voigt and Reuss models. Note that the absolute percentage standard errors of Kroner model fitting are 2.46 %, 6.34 %, 3.15 %, and 8.85 % for RT, 500 °C, 700 °C and 900 °C, respectively, showing the acceptable accuracy of the estimated single-crystal elastic constants. In fact, these two theoretical models only consider homogenous strains (Voigt) or stresses (Reuss) in all the grains during continuous loading. On the other hand, the Kroner model accounts for the variation of stresses as well as strains among all the grains. Thus, the Kroner's self-consistent model, which is the most suitable-applied calculation method to determine the macroscopic elastic moduli from diffraction elastic moduli for HEA systems (19, 20), was applied to the lattice-strain evolution results to obtain the macroscopic elastic moduli. The detailed calculation processes for the Kroner model are described in the Supplementary Section S1.

The calculated single-crystal elastic constants, C_{ij} , macroscopic elastic (E_M), shear (G_M), bulk (K_M) moduli, and Poisson's ratio (ν) at room and elevated temperatures are listed in Table 1. As the temperature increases up to 700 °C, the variation in C_{11} is more pronounced, as compared with C_{12} and C_{44} . These results suggest that a longitudinal strain significantly induces a change in



volume. This change in the volume is strongly associated with the temperature, and thus, corresponds to a relatively-large change in C_{11} . Consequently, the tetragonal shear modulus, $C' = [(C_{11} - C_{12})/2]$, is significantly reduced with the gradually-decreasing elastic, shear, and bulk moduli. Moreover, compared with the elastic constants at 700 °C, the values of C_{11} and C_{12} are drastically reduced at 900 °C, while C_{44} remains nearly constant at RT, 500 °C, 700 °C, and 900 °C, resulting in a small change in the tetragonal shear modulus, C'. This result implies the elastic stability of this BCC HEA against the tetragonal shear deformation.

Further analysis of the elastic moduli was performed, using the RUS. The elastic constants, C_{ij} , were determined from \sim 45 resonances where the frequencies ranged from 100 to 650 kHz, employing an iteratively-inverse fitting process of the measured resonances. A typical RUS resonance spectrum obtained from the NbTaTiV refractory HEA is shown in the Supplementary Fig. S1, in which the inset presents an example of Lorentz fitting of a single resonance peak. The obtained values of the elastic moduli for the NbTaTiV alloy are summarized in Table 1, showing good agreement with the in-situ neutron data.

Predictions of elastic moduli for the NbTaTiV refractory HEA via first-principles calculations

Based on the experimental observations of the elastic-deformation behavior for the NbTaTiV alloy, first-principles calculations are employed to theoretically confirm the values of single-crystal elastic moduli at RT, using the density functional theory (DFT). The Young's, bulk, and shear moduli at - 273 °C and RT for the current HEA are quantitatively calculated from the elastic constants determined by fitting ab-initio calculated stresses that correspond to the strained structures. The calculated and measured bulk elastic moduli at absolute zero temperature and RT are summarized in Table 1, which show good agreement between experimental and



theoretical results. The calculated-elastic moduli at RT were less than the experimentally-measured values by approximately -15.9%, -16.6%, and -6.0% for the Young's, shear, and bulk moduli, respectively. The above result corroborates the general trend of decreased stiffnesses in metals with increasing temperature. Furthermore, the calculated elastic constant values for C_{11} , C_{12} , and C' all decrease from absolute zero to RT, while C_{44} slightly increases from 31.6 GPa to 33.5 GPa.

The elastic properties of the NbTaTiV HEA were analyzed and plotted with respect to the crystallographic orientation, as illustrated in Fig. 3. To compute the direction-dependent elastic properties, tensorial operations were applied to the fourth order elastic tensor determined from the DFT calculations. The fourth-order elasticity tensor is transformed in a new basis set to determine elastic properties in any direction using the equation below.

$$C'_{\alpha\beta\nu\delta} = \lambda_{\alpha i} \,\lambda_{\beta i} \,\lambda_{\nu k} \,\lambda_{\delta l} \,C_{iikl} \tag{3}$$

where each λ is a directional cosine of the angle between the rotated and reference axes (21).

A higher degree of isotropic-elastic properties results in the smaller variation in the magnitude of the three-dimensional (3D) surfaces and two-dimensional (2D) contours. The 2D-contour plots correspond to a cut through the 3D surface plots on the XY, XZ, and YZ planes. The Young's modulus is represented by a solid surface with a color-map in which darker colors denote smaller values, and brighter colors indicate larger values. The maximum to the minimum Young's modulus ratio is 1.16, indicating little anisotropy characteristic. The maximum value of 107.7 GPa corresponds to the <100> direction, while the minimum value for the <111> is 93.0 GPa (see Figs. 3A and B). The 3D-surface plot for the linear compressibility is represented by a translucent green sphere, which exhibits negligible anisotropy since it has a value of 2.42 TPa⁻¹ in all directions (Figs. 3C and D). The range of the minimum and maximum values of the shear



moduli and Poisson's ratios for each direction of the applied stress is attributed to the variation in the direction of the measurement. In the 3D-surface plots of the shear modulus and Poisson's ratio, the translucent green surface represents the maximal values and envelopes the solid surface inside, which represents the minimal values. The minimum surface has a color-map applied such that darker colors represent smaller values than brighter colors, as illustrated in Figs. 3E and G. In the 2D plots, the maximum values are represented by a green curve, and the minimum values are denoted by a pink curve. The ratio of the maximum to the minimum shear modulus values is 1.17. The maximum is in the <111> direction with a value of 39.33 GPa, whereas the minimum corresponds to the <110> directions with a value of 33.51 GPa. Furthermore, the ratio of the maximum Poisson's ratio to the minimum ratio is 1.32. The maximum and minimum values both occur in the <110> direction with values of 0.44 and 0.33, respectively (Figs. 3F and H).

Recently, Ranganathan *et al.* (22) introduced a measurement method of anisotropy, using the universal elastic-anisotropy index, which can generally be applied to crystal systems that consider the bulk component of the elastic tensor. As opposed to other anisotropy measurement methods, such as the Zener anisotropy index, which is only applicable to cubic crystals, and the Ledbetter-Migliori anisotropy index, which only considers the shear component of the elastic tensor, the universal anisotropy index is given by the following equation

$$A^{U} = \frac{5G^{V}}{G^{R}} + \frac{K^{V}}{K^{R}} - 6 \ge 0 \tag{4}$$

where G is the shear modulus, K is the bulk modulus, and the V and R superscripts refer to the Voigt and Reuss estimates, respectively. As a comparison, the A^U values of the constituent elements obtained from the Materials Project database are Nb: 2.71, Ta: 0.07, Ti: 0.27, and V: 3.42. As a result, the A^U value for the NbTaTiV HEA is 0, which defines the single-crystal elastic properties to be isotropic.



2

3

4

5

6

7

8

9

10

11

12

13

14

15

16

17

18

19

20

21

22

23

Predictions of elastic moduli for the NbTaTiV refractory HEA via machine-learning (ML) models

The set of elemental and structural properties that were found to be good predictions in the shear modulus ML model were the Holder mean (4th power) of the group numbers of the elements, cohesive energy, the Holder mean (2nd power) of the atomic radii of the elements, the Holder mean (4th power) of the electronegativity of the elements, and density. The set of elemental and structural properties that were found to be good predictions in the bulk modulus ML-model were the Holder mean (4th power) of the group numbers of the elements, cohesive energy, the Holder mean (1st power) of the atomic radii of the elements, Holder mean (negative 4th power) of the electronegativity of the elements, and density. The ML-models' performance was tested on 20 % of the dataset, which was never seen by the ML-model during the fitting process. The bulk and shear moduli were log-normalized for model training and testing to ensure that large outlier values do not have an exaggerated effect on the models. The modelperformance metric used was the mean-squared error. The mean-squared error of the shear modulus and bulk-modulus models were 0.0409 and 0.0284, respectively. The ML-model predictions, compared with experimentally- and DFT-calculated values, are summarized in Table 1. The predicted shear modulus is 36.6 GPa, and the predicted bulk modulus is 146.3 GPa, giving relative errors of 2.5 % and 6 %, respectively.

There is also the stochastic variability in the model performance, depending on how the training dataset is shuffled. To determine the variability of model performance that is simply due to which training examples are included in the training dataset, learning curves are plotted in Fig. 4. The variability in model predictions due to the random shuffling of data is studied by randomly-shuffling the data in 20 different ways. The red curves represent the cross-validation



mean-squared error of the models during training averaged over the 20 different trials, and the green curves denote the mean-squared error of the models calculated on the testing set averaged over the 20 different trials. The shaded areas represent one standard deviation above and below, as determined from the 20 different trials. The x-axis of the learning curves shows how the size of the training dataset itself affects the model performance. The learning curves indicate that the model-prediction performance on the testing set converges after 3,000 training samples. The small difference in the training and testing mean-squared errors indicate that the model is sufficiently good at predicting the shear and bulk moduli for compounds that were not in the training dataset. This trend also illustrates the generalizability of the model in the sense that it can be used on compounds, which are not included in the original dataset.

DISCUSSION

Elastic isotropy and anisotropy deformation behaviors of the NbTaTiV refractory HEA

Typically, the response of lattice strains under applied stresses is strongly associated with the oriented grains due to the effects of elastic anisotropies in polycrystalline metal materials (12, 13), including FCC-structured HEAs (23). The elastically-anisotropic deformations originate from the orientation-dependent elastic modulus, which is presented by the different slopes in the plots of the lattice-strain evolution as a function of applied stresses. In the case of BCC structural materials, the {110} and {211} oriented grains, which possess higher elastic stiffnesses, exhibit the larger slopes. The {200} and {310} grains, on the other hand, possess smaller slopes with lower elastic stiffnesses (12, 18). After this elastic stretch, the sequence of grain yielding depends on the value of the Schmid factor, showing varying stress levels for the onset of yielding in differently-oriented grains, which is commonly characterized as the grain-to-grain yielding behaviors (18). The plastic anisotropy is derived from the occurrence of plastic deformation on



2

3

4

5

6

7

8

9

10

11

12

13

14

15

16

17

18

21

22

certain (hkl)-oriented grains, on which slip is preferred to occur. An increase in the slope indicates plastic yielding of particularly-oriented grains, whereas the reduction of the slope represents an intergranular load transfer from the yielding grains to the neighboring grains, which are still in the elastic-deformation region. With these lattice-strain evolution trends, {110} and {211}-oriented grains with the largest stiffnesses in the elastic region tend to yield at the early stage due to their slip system. Subsequently, a load transfers from the aforementioned grains to the {200} and {310}-oriented grains, resulting in an increase in the lattice strains during plastic deformation. Interestingly, unlike conventional BCC alloys, as discussed above, the NbTaTiV BCC refractory HEA exhibits no orientation-dependent lattice-strain evolutions during elastic deformation at RT, leading to nearly-similar values of elastic moduli in differentlyoriented grains, as presented in Fig. 2A. With this unusual elastic deformation, all orientated grains yield at the same stress level (around 1,000 MPa). Furthermore, the features of the load transfer were not clearly presented in the figure, indicating less anisotropic behavior during plastic deformation at RT. This trend reduced plastic anisotropic-deformation behavior could result in excellent ductility at RT due to the homogenous load sharing between differentlyoriented grains.

The elastic isotropy is often quantitatively described by the Zener anisotropy (A_z) ratio and Voigt and Reuss bounds (A_{VR}) :

$$A_{Z} = \frac{2C_{44}}{C_{11} - C_{12}} \tag{5}$$

$$A_{VR} = \frac{G_V - G_R}{G_V + G_R} \tag{6}$$

where $G_R = [5(C_{11} - C_{12}) \ C_{44}] / [4C_{44} + 3(C_{11} - C_{12})]$ and $G_V = (C_{11} - C_{12} + 3C_{44}) / 5$ (24). The calculated values of A_Z and A_{VR} at elevated temperatures can be found in the Supplementary



2

3

4

5

6

7

8

9

10

11

12

13

14

15

16

17

18

19

20

21

22

23

Table S2. In the case of ideal isotropic materials, the value of the tetragonal shear modulus (C') will be identical to the cubic shear modulus (C_{44}), and it results in $A_z = 1$ and $A_{VR} = 0$ (8, 11). Typically, the Zener ratios for most of the conventional FCC and BCC structural materials are well over 2.0 or 3.0, indicating the significant elastic anisotropy (23, 25). Recently, Tian et al. suggested an alloy-design strategy to achieve the elastic isotropy in HEAs using ab initio calculations (8). It was reported that the Mo-containing BCC refractory HEAs have the same polycrystalline shear and Young's moduli along all orientations, indicating elastic isotropy. Furthermore, these isotropic HEAs possess a similar valence electron concentration (VEC) of about 4.7 (generally, HEAs tend to form BCC solid-solution phases when VEC becomes less than 7.55) (8, 26), which is similar to other elastic-isotropy alloys, such as the Ti-V alloy (Gum Metals) (27). However, their reported works have strongly focused on only theoretical calculations, due to the lack of experimental verifications. According to our calculated results of Az and AvR in the Supplementary Table S2, which are primarily obtained from the in-situ neutron experiments, the NbTaTiV refractory HEA manifests almost perfectly-isotropic elastic deformation at RT ($A_Z \approx 1.2$, $A_{VR} \approx 0.0056$, and VEC ≈ 4.68). Moreover, the elastic isotropy was gradually increased at elevated temperatures. Many conventional alloys show the strong temperature-dependent elastic anisotropic-deformation behavior, indicating a significant increase of the Zener anisotropy parameters at higher temperatures (12, 13, 25). For example, the nanostructured BCC ferritic alloy (NFA) and FCC-structured Ni-based superalloy exhibited the large variation of anisotropy parameters from room to high temperatures [from 1.7 (RT) to 5.3 (800 °C) for NFA and from 2.8 (RT) to 3.6 (700 °C) for a Ni-based superalloy (13, 25). In case of the present NbTaTiV HEA, the Zener anisotropy parameters were gradually increased at elevated temperatures but the variation of anisotropy parameters in NbTaTiV (1.2 at RT and 1.6



at 900 °C) is smaller than other conventional alloys (12, 13, 25). The detailed comparisons of the Zener anisotropy parameters and yield strengths at elevated temperatures between the nanostructured ferritic alloy (13) and the present NbTaTiV refractory HEA are indicated in the Supplementary Fig. S2, manifesting that both alloys show the temperature-dependent elastic anisotropy and the smaller variation of the Zener anisotropy parameters in the NbTaTiV HEA than the nanostructured ferritic alloy at elevated temperatures.

Mechanical stability and ductility of the NbTaTiV refractory HEA

The mechanical stability of the NbTaTiV refractory HEA can be evaluated, considering the values of single-crystal elastic constants. Born and Huang (28) suggested the evaluation criteria of the elastic stability through the dynamical-stability conditions, $C_{11} > |C_{12}|, C_{11} + 2C_{12} > 0, \land C_{44} > 0$ (29). According to the elastic constants in Table 1, the present alloy shows good mechanical stability in all temperature ranges.

The intrinsic brittle/ductile deformation behavior of HEAs, which dominantly consists of solid-solution phases, can be predicted by the interrelation of polycrystalline elastic moduli, such as the Cauchy pressure $(C_{12}-C_{44})$ (14), Pugh ratio [bulk modulus (K) / shear modulus (G)] (9), and Poisson's ratio (v) (10). The Cauchy pressure (CP) is often used to categorize the type of atomic bonding. The relatively-large positive CP value represents an increased degree of the metallic-bonding character with the ductile-deformation behavior, while the negative CP stands for covalent bonding with brittle behavior (14). Moreover, Pugh suggested that the K/G ratio can be applied to predict the ductility and brittleness of materials (9). The brittle-to-ductile transition point $(K/G)_0$ is 1.75, which is established by the experimental results for a large number of studied materials. Higher values of Pugh ratios (> 1.75) indicate that the materials are ductile, whereas lower values are related to the brittle property (29). Based on the empirical criteria of



2

3

4

5

6

7

8

9

10

11

12

13

14

15

16

17

18

19

20

21

22

23

the Pugh ratio above, the ductile/brittle limit can also be assessed by the Poisson's ratio, considering the relationship between v and $(K/G)_0$, as v = (3K - 2G)/[2(3K + G)], in the case of isotropic polycrystalline materials. Therefore, the brittle-to-ductile transition limit, $(K/G)_0 > 1.75$, corresponds to v > 0.26. Note that the brittle-ductile criterion for bulk metallic glasses is v > 0.31 (10, 30). The values for the Cauchy pressure, Pugh ratio, and Poisson's ratio (see Tables 1 and the Supplementary Table S2), which are obtained from in-situ neutron experiments, suggest that NbTaTiV is intrinsically ductile.

Characterization of mobile dislocations for the NbTaTiV alloy at elevated temperatures.

In order to further investigate the plastic-deformation behaviors of the NbTaTiV alloy, the line-profile modeling and analyses, considering the evolution of the neutron-diffraction peak width, are carefully performed as a function of the macro-strain at elevated temperatures. In general, plastic deformation often leads to significant broadening of diffraction peaks, which is mostly caused by the formation of inhomogeneous strain fields (31). It is well known that the inhomogeneity of the sub-grain structure is usually more related to the accumulation of dislocations than variations of intergranular strains. Thus, it gives rise to strain fluctuations with the strain field around dislocations responsible for diffraction peak broadening (32). With the above fundamental understanding of the plastic-deformation behavior in metal materials, evolutions of diffraction-peak widths at different strain levels for the NbTaTiV refractory HEA are further discussed by the Williamson-Hall peak-broadening analysis approach (15). The evolution of the peak widths of the full-width-half-maximums (FWHM/FWHM₀) of {110}, {200}, {211}, and {310} diffraction peaks as a function of macro-strain at RT, 700 °C, and 900 °C, and the detailed processes of the Williamson-Hall peak-broadening analysis during plastic deformation are described in the Supplementary Section S2 (33).



Figure 5 shows the modified Williamson-Hall plots for the NbTaTiV alloy corresponding to the macro-strain range from 0 to 15 %. The response of linear fitting of the plot, which is obtained from the assumption of specific types of dislocations, refers to the dominant mobile dislocation character during plastic deformation (34). Hence, when treating q and C_{h00} values as pure screw dislocations \dot{c} , the non-monotonous deviation of ΔK as a function of K^2C gradually increases with an increase in the macro-strain, as exhibited in Fig. 5A. Nevertheless, the data follows a linear trend at all strain levels, when the values of ΔK and K^2C obtained with the pure edge-dislocation consideration $|q=0.0673 \land C_{h00}=0.1937|$, as exhibited in Fig. 5B. The deviations from the linear-fitted line are quantitatively described by R-squared coefficients in the Supplementary Table S4. These results clearly indicate that the type of mobile dislocations of the NbTaTiV refractory HEA are edge dislocations in the initial condition (non-deformed) at elevated temperatures. Moreover, with increasing macro-strains (up to 15 % deformed), the <111> {110} edge dislocation remains as a dominant mobile dislocation character at room and elevated temperatures (Figs. 5B to D)

The BCC metallic materials, typically, contain edge dislocations, which move faster than screw dislocations due to their core properties of dislocations during plastic deformation (35). The critical stress, which forces the edge-dislocation movement, is quite small (< 10 MPa for the pure BCC Fe), leading to the easy annihilation of the edge dislocations, which results in the screw/edge anisotropy in the apparent mobility deviation (35). Therefore, the remaining dislocations tend to have more screw character in BCC metals. Recently, however, Rao et al. (36) have reported atomistic simulations of plastic-deformation behavior for the BCC HEA in terms of dislocation motion. This in-depth investigation predicts the tendency of dislocation motions in the BCC solid-solution HEA to correspond to the random elemental distribution,



which is considerably different from conventional BCC metals. During the plastic deformation, the edge-dislocation core can be deviated from their neutral dislocation planes, producing the wavy dislocation lines, which are attributed to the severe lattice distortion. This feature is induced by compositional fluctuations and thus, leads to not only strengthening but also significant difficulty in the edge-dislocations movement. These predictions of plastic-deformation behavior for the BCC HEA suggest that the number of edge dislocations is comparable to that of the screw dislocations, which is in contrast to the conventional low-entropy BCC metals. Similar to the above reported prediction, the dominant mobile dislocations of the investigated NbTaTiV BCC refractory HEA, which has severely distorted lattices, are close to <111> {110} edge dislocations with increasing macro-strain, as presented in Fig 5B.

In order to further identify and provide visible evidence of the type of mobile dislocations, during plastic deformation in the NbTaTiV HEA, the nano-scale microstructure of the deformed sample was carefully investigated with the TEM study. Figure 5E exhibits the filtered HAADF-STEM image of the 15 % RT-deformed NbTaTiV HEA, which are acquired along the [110] zone axis. The formation of edge dislocations is clearly observed with extra planes on the image, described by the symbol "L", which is consistent with line-profile modeling, using Williamson-Hall plot results (Figure 5B). It is found that these edge dislocations were formed on different oriented planes, indicated by different colored symbols of edge dislocations. The high-magnification image of Fig. 5E is illustrated in Fig. 5F to provide a clear description of the edge dislocations.

CONCLUSIONS

Overall, this comprehensive study provides evidence for the unique elastic and plastic deformation behavior of the single BCC solid-solution phase refractory HEA at elevated



temperatures, using in-situ neutron experiments coupled with theoretical calculations. The results of the neutron-diffraction and characterization of the microstructure show the excellent BCC single-phase stability up to 900 °C. Furthermore, the present alloy possesses 全 high yield strength and excellent plasticity at RT as well as softening resistance at elevated temperatures. The lattice-strain-evolution results show the distinctive elastic-deformation behavior as an elastic isotropy at RT, and temperature-dependent elastic anisotropic-deformation behavior at elevated temperatures.

The single-crystal elastic moduli are obtained from the in-situ neutron-diffraction data coupled with the Kroner-model approach, showing excellent agreement with the experimental values determined from RUS measurements and first-principles calculations. Furthermore, the good agreement of the ML-model predictions of shear and bulk moduli is somewhat surprising, given that the Materials Project database only contains ordered compounds and does not contain disordered alloys, such as HEAs. The lattice-distortion effect may also cause the ML model to produce less accurate results for the HEAs, but given the lack of data for comparison, the good agreement suggests that these models may be useful for conservative estimates.

The NbTaTiV alloy is predicted to be intrinsically ductile, based on the ductility criteria, using the Cauchy pressure, Pugh ratio, and Poisson's ratio. The verification of the mobile dislocation type was quantitatively investigated, using the Williamson-Hall plot profile, experimentally verified by HAADF-STEM. The dominant mobile dislocation is determined to be the character of edge dislocations during the 15 %-plastic deformation at elevated temperatures. It is thought that the severely-distorted lattice induces the deviation of the formation of dislocations from their neutral dislocation planes, which consequently, leads to a significant reduction in the mobility of edge dislocations during plastic deformation. Thus, the edge



dislocations are believed to be the dominant dislocation type for the BCC refractory HEA, which is atypical, as compared to the conventional BCC metals and alloys. These new discoveries of unique elastic and plastic deformation behaviors of the BCC NbTaTiV refractory HEA may lead to the overall excellent mechanical performance and also provide a road map towards the discovery and production of newly-designed polycrystalline materials for structural-materials applications.

MATERIALS AND METHODS

Materials preparation and microstructural characterization

The alloys were synthesized by arc-melting under an argon atmosphere on a water-cooled Cu hearth from Nb, Ta, Ti, and V elements of 99.99 weight percent (wt. %) purity. The nominal composition of the present alloy is Nb₂₅Ta₂₅Ti₂₅V₂₅ in atomic percent (at. %). The ingot was melted over 10 times to ensure a fully-homogeneous distribution of elements. From the master alloys, the specimens were fabricated, followed by direct casting into cylindrical rods with a 4-mm diameter and 50-mm length, using a drop-casting technique. These alloys were sealed with the triple-pumped argon in quartz tubes and homogenized at 1,200 °C for 3 days, followed by water cooling. The microstructure was examined by scanning-electron microscopy (SEM), using a Zeiss Auriga 40 equipped with back-scattered electrons (BSE). The chemical analysis of the alloy was studied by the energy-dispersive X-ray spectroscopy (EDS) after the homogenization treatment.

In-situ neutron diffraction experiments

The in-situ neutron-diffraction (ND) measurements were carried out on the VULCAN Engineering Diffractometer at the Spallation Neutron Source (SNS) facility located at the Oak Ridge National Laboratory (ORNL). The ND instrument utilizes the time-of-flight (TOF)



2

3

4

5

6

7

8

9

10

11

12

13

14

15

16

17

18

19

20

21

22

23

measurements, which allows for the development of the neutron-diffraction pattern, covering a wide range of d-spacings without the rotation of detectors or samples. The two detectors, which are designated as Banks 1 and 2 at +/-90 degrees, were employed to collect diffracted neutrons from the polycrystalline grains with lattice planes parallel to the axial and transverse directions, respectively. The compression experiments on the homogenization-treated NbTaTiV alloy with a diameter of 4 mm and length of 8 mm were conducted to investigate the elastic and plastic deformation behaviors at room and elevated temperatures, using a mechanical-testing system (MTS) load frame. The samples are illuminated by the incident neutron beam of a 3×3 mm² slit size and 2-mm receiving collimators. During the elastic-deformation period, a stepwise-force control sequence was utilized by collecting the 20 mins, measurement time of neutron-diffraction data at each stress level. When the stress level reached 1,030 MPa for RT, 650 MPa for 500 °C, 585 MPa for 700 °C, and 550 MPa for 900 °C (close to the macroscopic yield strength), respectively, a stepwise displacement control with an incremental step of 0.2 mm was employed. The collected data were analyzed by single-peak fitting, using the VULCAN Data Reduction and Interactive Visualization software (VDRIVE) program (16).

First-principles calculations

First-principles calculations were performed with the Vienna Ab-initio Simulation Package (VASP), using the projector augmented wave (PAW) method (37). The exchange-correlation energy was described with the generalized gradient approximation (GGA) in the Perdew-Becke-Ernzehof (PBE) parameterization. A plane-wave cutoff of 700 eV and Monkhorst-Pack k-point grid of $4 \times 4 \times 4$ was used for all calculations. The chemical disorder of the solid solution was modeled using a 64 atom Special Quasirandom Structure (SQS). The SQS was employed, using a method based on a Monte Carlo-simulated annealing loop where atomic



configurations are proposed by randomly-swapping atomic positions and accepting changes when the configuration's calculated correlation functions are a closer match to that of a disordered state.

The elastic tensor of the SQS supercell was calculated, using a set of distorted structures based on the methodology described in the reference (38). The supercell's lattice parameters were fixed at the experimentally-determined RT values, and the ionic positions were allowed to relax. A set of deformed structures were generated by adopting 3×3 Green-Lagrange strain tensors of varying magnitudes at $\pm 0.5\%$ and $\pm 1\%$. For each distorted structure, the 3×3 stress tensor is computed by the density functional theory (DFT). A linear least-squares fit between the stress and strain tensors was performed to calculate the elastic tensor of the SQS. However, since the SQS supercell does not conserve the point-group symmetry, a projection technique is used to derive the closest elastic tensors with a cubic symmetry for the NbTaTiV alloy, which is equivalent to crystallographically-averaging tensor elements. The projection method is computationally-efficient, and the elastic constant values converge quickly with the size of SQS. The elastic moduli of the current HEA are calculated, using the elements of the projected elastic tensor, as described below. The bulk modulus (K) and shear modulus (G& were obtained from the elastic constant. Then Young's modulus was mathematically calculated, substituting K and

G in the simple equation $(E = \frac{9KG}{3K+G})$, which considered the correlation among E, K, and G.

$$K = \frac{5}{\left(s_{11} + s_{22} + s_{33}\right) + 2\left(s_{12} + s_{23} + s_{31}\right)}$$
 (7)

$$20 \qquad G = \frac{15}{4(s_{11} + s_{22} + s_{33}) - 4(s_{12} + s_{23} + s_{31}) + 3(s \square_{44} + s_{55} + s_{66})} + \frac{(s_{11} + s_{22} + s_{33}) - (s_{12} + s_{23} + s_{31}) + 3(s \square_{44} + s_{55} + s_{66})}{15}$$



where s_{ij} is the stiffness tensor, and the elastic tensor, C_{ij} , was calculated, following their correlation, $s_{ij} = C_{ij}^{-1}$.

Machine-learning (ML) models for bulk and shear moduli

Machine-learning (ML) models using the gradient-boosted trees algorithm were developed to predict shear and bulk moduli (one model for each). Models were built using the Scikit-Learn library in Python (39). The ML models were trained on DFT-calculated shear and bulk moduli, elemental properties, and compound structural properties from the Materials Project database (38). There were 6,826 inorganic compounds in the dataset used for training and testing the ML models. The most general approach to combining elemental properties for each compound was taken by computing the compositionally-weighted Holder means with a range of powers from -4 to 4. The Holder means are defined in the equation below:

$$\mu_{p}(x) = \left(\left(\sum_{i=1}^{n} w_{i} \right)^{-1} \sum_{i=1}^{n} w_{i} x_{i}^{p} \right)^{\frac{1}{p}}, \quad (p \neq 0)$$
(9)

$$\mu_0(x) = \exp\left(\left(\sum_{i=1}^n w_i\right)^{-1} \sum_{i=1}^n w_i \ln\left(x_i\right)\right), (p=0)$$
(10)

where μ_p is the Holder mean with the power, p; w_i is the compositional fraction of the element, i, in a compound with n elements. A Holder mean with the powers of 1, -1, or 2 corresponds to the arithmetic mean, harmonic mean, or Euclidean mean, respectively. A feature selection methodology based on a genetic algorithmic optimization scheme was utilized to determine which Holder means of which elemental properties and structural properties result in the best predictive models for shear and bulk moduli. The models were trained using 80% of the dataset with a 5-fold cross-validation scheme to prevent overfitting. The model performance is determined on the remaining 20% of the dataset.



Resonant Ultrasound Spectroscopy

Elastic constants were also measured using Resonant Ultrasound Spectroscopy (RUS). A cylindrical sample of the NbTaTiV HEA was corner mounted between two transducers. In this configuration, one transducer excites the sample while a receiving transducer detects and relays the sample's response of resonant frequencies. Assuming the elastic isotropy, the elastic constants, C_{11} , C_{12} and C_{44} , were determined, using sample dimensions, and observed resonances. In our study, the frequency was swept through the 100 - 650 kHz range with large responses detected when the frequency corresponds to an eigenfrequency of the sample. From the elastic constants, bulk modulus (B) and shear modulus (G) were determined, using Hill's approximations (40).

REFERENCES AND NOTES:

- 1. Z. Li, K. G. Pradeep, Y. Deng, D. Raabe, C. C. Tasan, Metastable high-entropy dual-phase alloys overcome the strength–ductility trade-off. *Nature* **534**, 227-231 (2016).
- 2. B. Gludovatz *et al.*, A fracture-resistant high-entropy alloy for cryogenic applications.

 22 Science **345**, 1153-1158 (2014).



- 3. C. Lee *et al.*, Lattice Distortion in a Strong and Ductile Refractory High-entropy Alloy.
- 2 Acta Materialia **160**, 158-172 (2018).
- 3 4. B. Cantor, I. Chang, P. Knight, A. Vincent, Microstructural development in equiatomic
- 4 multicomponent alloys. *Materials Science and Engineering: A* **375**, 213-218 (2004).
- 5. C. L. Tracy *et al.*, High pressure synthesis of a hexagonal close-packed phase of the high-
- 6 entropy alloy CrMnFeCoNi. *Nature Communications* **8**, 15634 (2017).
- 7 6. Y. Zhang, *High-Entropy Materials: A Brief Introduction*. (Springer, 2019).
- 7. J.-W. Yeh et al., Formation of simple crystal structures in Cu-Co-Ni-Cr-Al-Fe-Ti-V
- 9 alloys with multiprincipal metallic elements. Metallurgical and Materials Transactions A
- **35**, 2533-2536 (2004).
- 11 8. F. Tian, L. K. Varga, N. Chen, J. Shen, L. Vitos, Ab initio design of elastically isotropic
- TiZrNbMoVx high-entropy alloys. *Journal of Alloys and Compounds* **599**, 19-25 (2014).
- 9. S. Pugh, XCII. Relations between the elastic moduli and the plastic properties of
- polycrystalline pure metals. *The London, Edinburgh, and Dublin Philosophical Magazine*
- and Journal of Science **45**, 823-843 (1954).
- 10. X. Gu, A. McDermott, S. J. Poon, G. J. Shiflet, Critical Poisson's ratio for plasticity in
- Fe-Mo-C-B-Ln bulk amorphous steel. *Applied Physics Letters* **88**, 211905 (2006).
- 18 11. H. Zhang et al., Elastic properties of Al x CrMnFeCoNi $(0 \le x \le 5)$ high-entropy alloys
- from ab initio theory. *Acta Materialia* 115, 12-22 (2018).
- 20 12. S. Huang et al., In situ neutron-diffraction studies on the creep behavior of a ferritic
- superalloy. *Metallurgical and Materials Transactions A* **43**, 1497-1508 (2012).



- 1 13. G. M. Stoica, A. D. Stoica, M. K. Miller, D. Ma, Temperature-dependent elastic
- anisotropy and mesoscale deformation in a nanostructured ferritic alloy. Nature
- 3 *Communications* **5**, 1-8 (2014).
- 4 14. D. G. Pettifor, Theoretical predictions of structure and related properties of intermetallics.
- 5 *Materials Science and Technology* **8**, 345-349 (1992).
- 6 15. G. Williamson, W. Hall, X-ray line broadening from filed aluminium and wolfram. *Acta*
- 7 *metallurgica* **1**, 22-31 (1953).
- 8 16. K. An, VDRIVE-Data reduction and interactive visualization software for event mode
- 9 neutron diffraction. ORNL Report No. ORNL-TM-2012-621 Oak Ridge National
- 10 Laboratory, Oak Ridge, TN, (2012).
- 17. J. H. Hollomon, Tensile deformation. *Aime Trans* 12, 1-22 (1945).
- 12 18. M. Daymond, H. Priesmeyer, Elastoplastic deformation of ferritic steel and cementite
- studied by neutron diffraction and self-consistent modelling. Acta materialia 50, 1613-
- 14 1626 (2002).
- 15 19. E. Kröner, Berechnung der elastischen Konstanten des Vielkristalls aus den Konstanten
- des Einkristalls. Zeitschrift für Physik **151**, 504-518 (1958).
- 17 20. R. De Wit, Diffraction elastic constants of a cubic polycrystal. *Journal of applied*
- 18 *crystallography* **30**, 510-511 (1997).
- 19 21. A. Marmier et al., ElAM: A computer program for the analysis and representation of
- anisotropic elastic properties. Computer Physics Communications 181, 2102-2115
- 21 (2010).
- 22. S. I. Ranganathan, M. Ostoja-Starzewski, Universal elastic anisotropy index. *Physical*
- 23 Review Letters **101**, 055504 (2008).



- 1 23. Y. Wu et al., In-situ neutron diffraction study of deformation behavior of a multi-
- 2 component high-entropy alloy. *Applied Physics Letters* **104**, 051910 (2014).
- 24. L. Vitos, The EMTO method and applications in computational quantum mechanics for
- 4 materials engineers. Springer-Verlag, London) Gyorffy BL, Stocks GM (1983)
- 5 Concentration waves and fermi surfaces in random metallic alloys. Phys Rev Lett 50,
- 6 374-377 (2007).
- 7 25. Z. Wang, A. D. Stoica, D. Ma, A. M. Beese, Diffraction and single-crystal elastic
- 8 constants of Inconel 625 at room and elevated temperatures determined by neutron
- 9 diffraction. *Materials Science and Engineering: A* **674**, 406-412 (2016).
- 10 26. S. Guo, C. Ng, J. Lu, C. Liu, Effect of valence electron concentration on stability of fcc
- or bcc phase in high entropy alloys. *Journal of applied physics* **109**, 103505 (2011).
- 12 27. T. Li, J. Morris Jr, N. Nagasako, S. Kuramoto, D. Chrzan, "Ideal" engineering alloys.
- 13 *Physical review letters* **98**, 105503 (2007).
- 14 28. M. Born, K. Huang, *Dynamical theory of crystal lattices*. (Clarendon press, 1954).
- 15 29. K. Gschneidner Jr et al., A family of ductile intermetallic compounds. *Nature Materials*
- **2**, 587 (2003).
- 17 30. J. Schroers, W. L. Johnson, Ductile bulk metallic glass. *Physical Review Letters* 93,
- 18 255506 (2004).
- 19 31. E. Francis *et al.*, High-temperature deformation mechanisms in a polycrystalline nickel-
- base superalloy studied by neutron diffraction and electron microscopy. *Acta Materialia*
- **74**, 18-29 (2014).
- 22 32. X.-L. Wang *et al.*, Inter-and intragranular stresses in cyclically-deformed 316 stainless
- steel. *Materials Science and Engineering: A* **399**, 114-119 (2005).



- 1 33. F. Maresca *et al.*, Edge Dislocations Can Control Yield Strength in Refractory Body-2 Centered-Cubic High Entropy Alloys. Submitted (2020).
- 3 34. T. Ungár, I. Dragomir, Á. Révész, A. Borbély, The contrast factors of dislocations in cubic crystals: the dislocation model of strain anisotropy in practice. *Journal of applied* crystallography **32**, 992-1002 (1999).
- D. Caillard, Kinetics of dislocations in pure Fe. Part I. In situ straining experiments at room temperature. *Acta Materialia* **58**, 3493-3503 (2010).
- 8 36. S. Rao *et al.*, Atomistic simulations of dislocations in a model BCC multicomponent concentrated solid solution alloy. *Acta Materialia* **125**, 311-320 (2017).
- 10 37. P. E. Blöchl, Projector augmented-wave method. *Physical Review B* **50**, 17953 (1994).
- 11 38. M. De Jong *et al.*, Charting the complete elastic properties of inorganic crystalline compounds. *Journal of Scientific Data* **2**, 150009 (2015).
- 13 39. F. Pedregosa *et al.*, Scikit-learn: Machine learning in Python. *Journal of Machine*14 *Learning Research* **12**, 2825-2830 (2011).
- 15 40. R. Hill, The elastic behaviour of a crystalline aggregate. *Proceedings of the Physical*16 Society. Section A 65, 349 (1952).

Acknowledgments:

- We would like to thank J. Brechtl, H. Choo, and Y. Chen for assistance with the experiments,
- 20 respectively.
- Funding:

17

- The research is supported by the U.S. Army Office Project (W911NF-13-1-0438 and W911NF-
- 23 19-2-0049) with the program managers, Drs. Michael P. Bakas, David M. Stepp, and S.



2

3

4

5

6

7

8

9

10

11

12

13

14

15

16

17

18

19

20

21

22

Mathaudhu, and the material was developed. Peter K. Liaw also thanks the support from the National Science Foundation (DMR-1611180 and 1809640) with the program directors, Drs. Judith Yang, Gary Shiflet, and Diana Farkas, and the neutron work was conducted. C. Lee and B.L. Musicó would like to acknowledge the partial support from the Center of Materials Processing with Prof. Claudia Rawn as the director, a Tennessee Higher Education Commission (THEC) Center of Excellence located at The University of Tennessee, Knoxville, A portion of research at the ORNL's Spallation Neutron Source was sponsored by the Scientific User Facilities Division, Office of Basic Energy Sciences, U.S. Department of Energy. Reference herein to any specific commercial product, process, or service by the trade name, trademark, manufacturer, or otherwise, does not necessarily constitute or imply its endorsement, recommendation, or favoring by the United States Government or any agency thereof. The views and opinions of authors expressed herein do not necessarily state or reflect those of the United States Government or any agency thereof. YC and YCC thank the funding from the Ministry of Science and Technology (MOST) of Taiwan under Grant No. MOST-109-2636-M-009-002, the core facility support at the National Chiao Tung University (NCTU) from MOST. YCC thanks the partial support from the "Center for the Semiconductor Technology Research" from The Featured Areas Research Center Program within the framework of the Higher Education Sprout Project by the Ministry of Education (MOE) in Taiwan and supported in part by the Ministry of Science and Technology, Taiwan, under Grant MOST 109-2634-F-009-029. MCG acknowledges the support of the US Department of Energy's Fossil Energy Cross-Cutting Technologies Program at the National Energy Technology Laboratory (NETL) under the RSS contract, 89243318CFE000003. Furthermore, the present work was supported by the Basic



- 1 Research Laboratory Program through the Ministry of Education of the Republic of Korea (No.
- 2 2019R1A4A1026125).
- 3 Disclaimer: This work was partially funded by the Department of Energy, National Energy
- 4 Technology Laboratory, an agency of the United States Government, through a support contract
- 5 with Leidos Research Support Team (LRST). Neither the United States Government nor any
- agency thereof, nor any of their employees, nor LRST, nor any of their employees, makes any
- warranty, expressed or implied, or assumes any legal liability or responsibility for the accuracy,
- 8 completeness, or usefulness of any information, apparatus, product, or process disclosed, or
- 9 represents that its use would not infringe privately owned rights. Reference herein to any specific
- 10 commercial product, process, or service by trade name, trademark, manufacturer, or otherwise,
- does not necessarily constitute or imply its endorsement, recommendation, or favoring by the
- 12 United States Government or any agency thereof. The views and opinions of authors expressed
- herein do not necessarily state or reflect those of the United States Government or any agency
- 14 thereof.

Author Contributions:

- All authors contributed extensively to the work presented in this manuscript. C.L., P.K.L., K.A.,
- and G.S. performed the scanning-electron-microscopy, in-situ neutron, and mechanical tests and
- wrote the main manuscripts and supplementary materials. M.C.G. designed the HEA and
- conducted the calculation of phase diagram and wrote the computational prediction parts in the
- 20 main manuscript. G.K. and W.C. conducted the first-principles calculations, machine learning
- and wrote the calculation parts in the main manuscript. Y.C. and Y.C.C. performed the high-
- angle-annular-dark-field-scanning-transmission-electron-microscopy and wrote the atomic-scale
- structure investigation parts in the main manuscript. B.L.M. and V.K. conducted the resonant



- 1 ultrasound spectroscopy measurement and wrote the corresponded parts in the main manuscript.
- 2 All authors discussed the results and implications and commented on the manuscript at all rages.

Competing Interests:

- The authors declare that they have no competing financial interests.
- 5 Correspondence and requests for materials should be addressed to P. K. L. (pliaw@utk.edu)

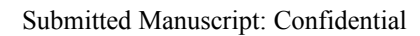
Data and Materials Availability:

- All data needed to evaluate the conclusions in the paper are present in the paper and/or the
- 8 Supplementary Materials. Additional data related to this paper may be requested from the
- 9 authors.

10

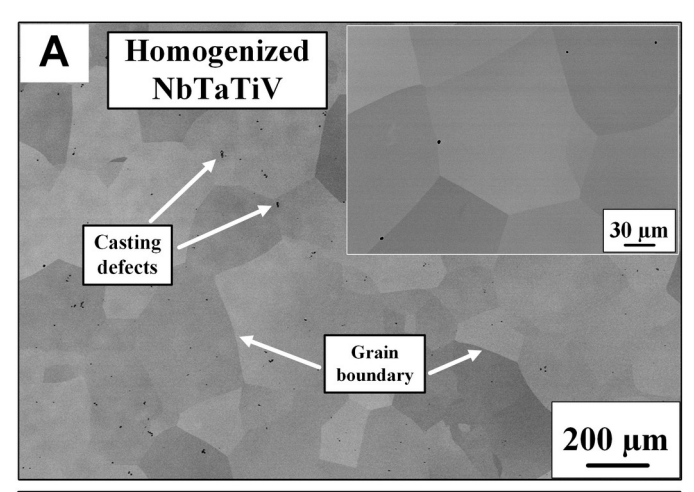
Supplementary Materials:

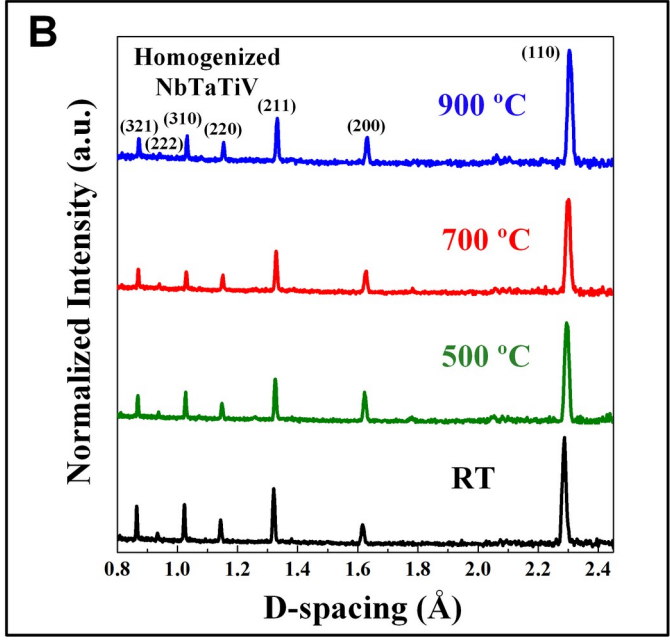
- Section S1. Calculations of single-crystal elastic constants, macroscopic Young's, shear, and
- bulk moduli from the in-situ neutron data with the Kroner model.
- Section S2. Plastic-deformation behaviors of the NbTaTiV alloy at elevated temperatures.
- Fig. S1. Resonance-ultrasound-spectrum result for the NbTaTiV refractory HEA.
- Fig. S2. Comparison of the Zener anisotropy parameter and yield strength at elevated
- temperatures between the nanostructured ferritic alloy and the present NbTaTiV refractory HEA.
- 17 Fig. S3. Evolution of the normalized full width at half maximum (FWHM/FWHM₀) as a function
- of macro-strain for the homogenized NbTaTiV alloy, obtained from the in-situ neutron
- 19 experiments at elevated temperatures.
- Table S1. The diffraction elastic moduli, E_{hkl} , of different crystallographic planes for the
- 21 homogenized NbTaTiV alloy at elevated temperatures.
- Table S2. Elastic-anisotropy factors (A_Z, A_{VR}, and VEC) and brittle-ductile criteria (K/G and
- Cauchy Pressure) for the homogenized NbTaTiV alloy at RT, 500 °C, 700 °C, and 900 °C.





1	Table S3. Substituting values (C_{h00} and q) for the dislocation contrast factor (C_{hkl}) to perform the
2	modified Williamson-Hall plots at RT, 700 °C, and 900 °C.
3	Table S4. R-squared coefficients, which is statistically obtained from the fitting of modified
4	Williamson-Hall plots for the homogenized NbTaTiV alloy at various temperatures and macro-
5	strains.
6	
7	
8	
9	
10	





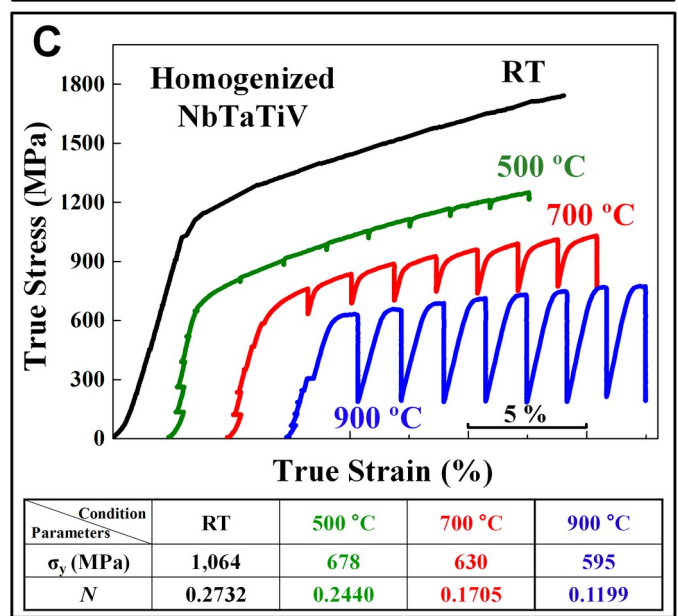




Fig. 1. Microstructures, phase characteristics, and mechanical properties of the homogenized
NbTaTiV alloy, studied by SEM, neutron diffraction (ND), and nominal compressive true strain-
stress curves during in-situ ND experiments at elevated temperatures. (A) SEM-BSE image of
the homogenization-treated NbTaTiV refractory HEA. (B) neutron-diffraction patterns with the
peaks indexed for a BCC structure at RT, 500 °C, 700 °C, and 900 °C, respectively. (C) True stress-
strain curves recorded during the in-situ compression experiment at RT, 500 °C, 700 °C, and 900
°C with a strain rate of 1×10^{-4} s ⁻¹ .

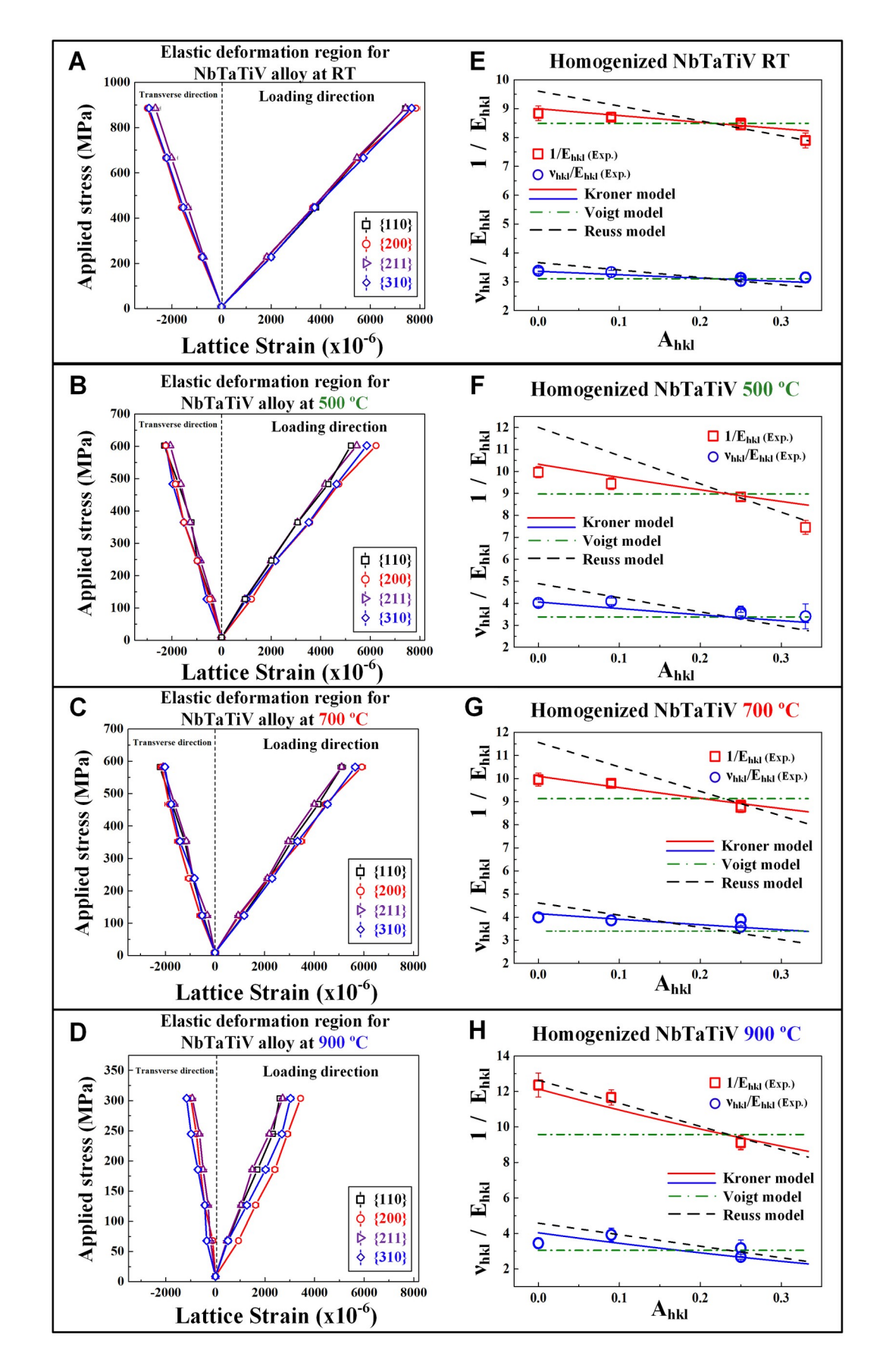




Fig. 2. Lattice-strain evolution in the NbTaTiV refractory HEA as a function of the applied stress, obtained from the in-situ ND experiments during the elastic deformation and plots of elastic moduli of differently-oriented crystals as a function of the elastic-anisotropy factor and fitting with the Kroner, Voigt, and Reuss models at RT, 500 °C, 700 °C, and 900 °C. The corresponding lattice strains of {110}, {200}, {211}, and {310} orientation planes along the axial and transverse directions during the elastic deformation (A) RT, (B) 500 °C, (C) 700 °C, and (D) 900 °C, respectively. The reciprocal diffraction elastic moduli ($1/E_{hkl}$ and v_{nkl}/E_{hkl}) as a function of the elastic-anisotropy factor, A_{hkl} ($\frac{h^2k^2+k^2l^2+l^2h^2}{[h^2+k^2+l^2]^2}$), which are obtained from the experimental elastic lattice strain (symbols) and fitted by Kroner, Voigt, and Reuss models (solid lines) at (E) RT, (F) 500 °C (G) 700 °C, and (H) 900 °C, respectively.

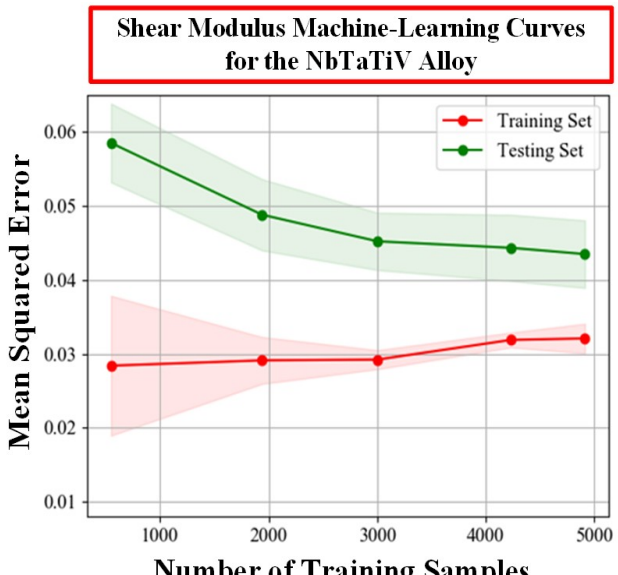


3D surface plot of 2D projection onto XY, directional elastic properties XZ, and YZ planes В Α 000/ Elastic Modulus 110 | 0 | GPa] 50 55 [0 1 0] 50 100 *E* [GPa] 50 100 50 C D Linear Compression 1.25 1.25 *LC*[*TPa* 2.5 1.25 1.25 F Ε Shear Modulus 40 G[GPa]17.5 20 17.5 G[GPa] 17.5 17.5 G Н 0.4 Poisson's Ratio 0.2 0.2 0 0.2 0.2 0.2 0.4 0.4 0.4 0.2 0.2 0.4 0.2 0 0.2 0.40.4 0.4



rig. 3. Directional dependence of inst-principles-calculated Ki elastic properties. The
magnitude with respect to the directions in three dimensions for (A) Young's modulus in GPa
(B) linear compressibility in TPa ⁻¹ , (C) shear modulus in GPa, and (D) Poisson's ratio, respectively
Shear modulus and Poisson's ratio are represented by two surfaces for maximum and minimum
values. The magnitude with respect to directions on the XY, XZ, and YZ planes for (E) Young's
modulus in GPa, (F) linear compressibility in TPa ⁻¹ , (G) shear modulus in GPa, and (H) Poisson's
ratio, respectively. Shear modulus and Poisson's ratio are represented by two lines for maximum
and minimum values.





Number of Training Samples

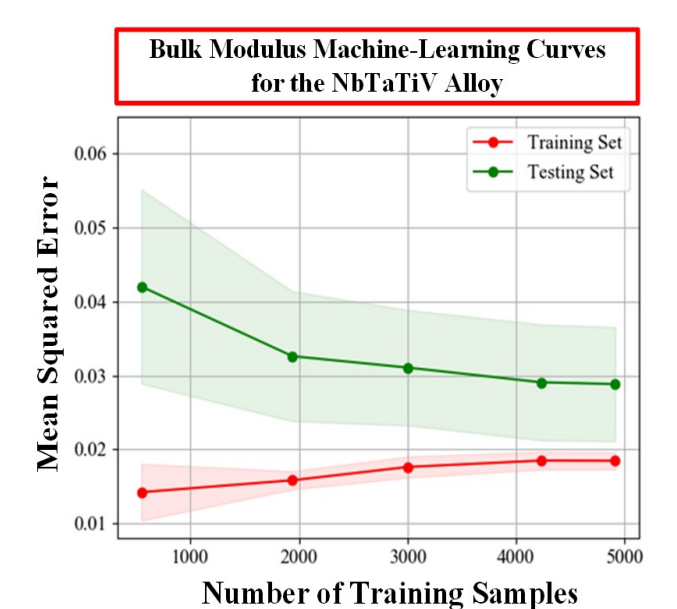




Fig. 4. Learning curves for shear and bulk moduli machine-learning models. The solid curves represent the means-squared error averaged over 20 different trials, and the shaded areas 2 represent one standard deviation above and below. The x axis represents the size of the training 3 dataset. The red curve and area correspond to the training phase, and the green curve and area 4 correspond to the testing phase.

6

5



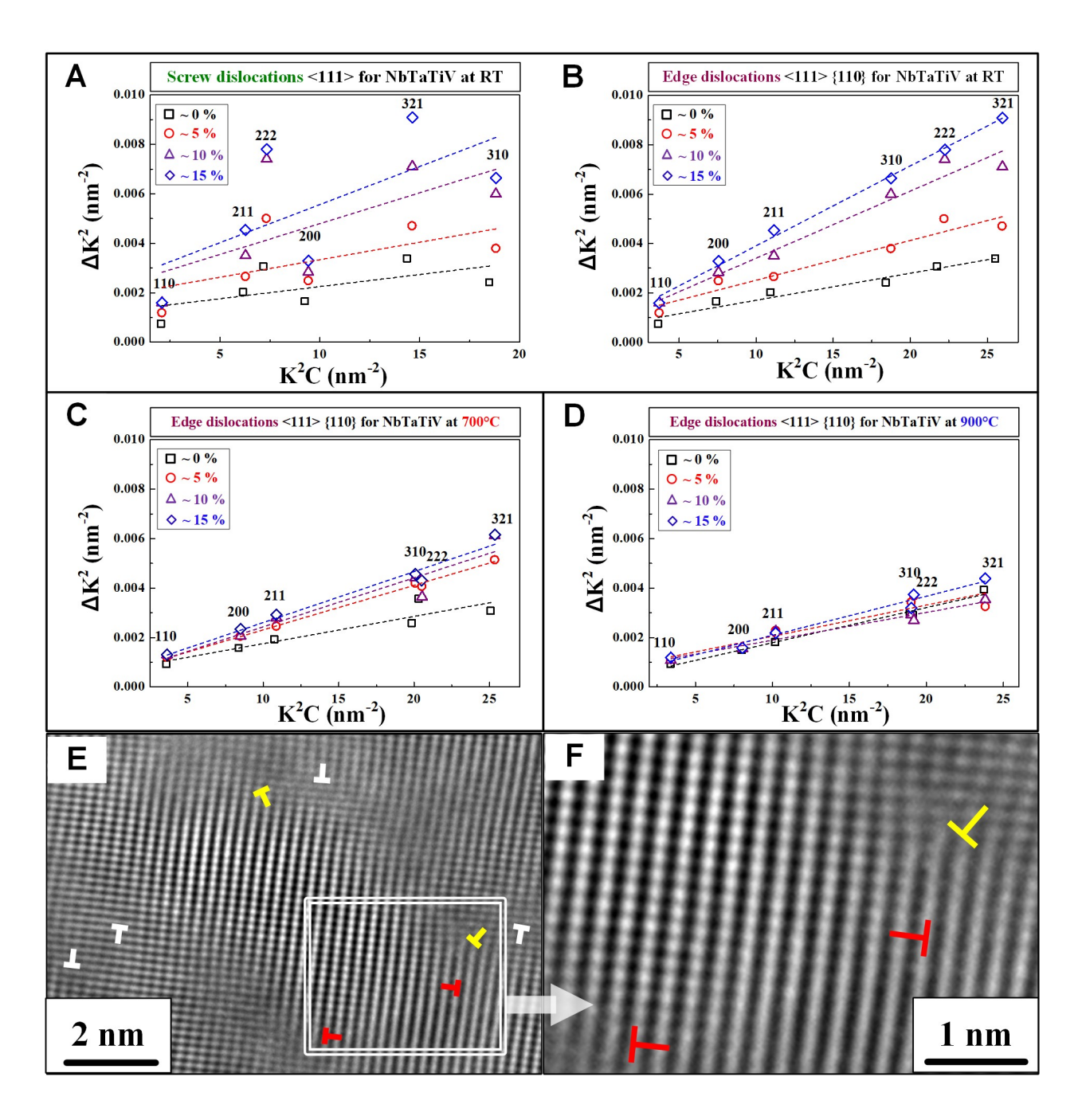




Fig. 5. Neutron-diffraction pattern line-profile modeling for the homogenized NbTaTiV alloy during plastic deformation, using the modified Williamson-Hall plot at elevated temperatures. HAADF-STEM images of the RT-deformed NbTaTiV alloy. The peak-broadening analysis, ΔK^2 , as a function of K^2C , for the sample compressed from 0 % to 15 %, considering the dominant type of dislocations as a pure (A) <111> screw dislocation at RT, (B) <111> {110} edge dislocation at RT, (C) <111> {110} edge dislocation at 700 °C, and (D) <111> {110} edge dislocation at 900 °C, respectively. (E) and (F) The visible investigation of the presence of edge dislocations for the 15 % RT-deformed NbTaTiV HEA by the HAADF-STEM study.



Parameters									
Conditions		(GPa)	C ₁₂ (GPa)	C ₄₄ (GPa)	C' (GPa)	E_M (GPa)	G_M (GPa)	K _M (GPa)	v
Contacto	In-situ neutron at RT	196.8	121.4	46.7	37.7	117.3	42.9	146.6	0.368
	In-situ neutron at 500 °C	190.5	129.9	46.0	30.3	107.6	38.9	150.1	0.382
Experi- mental Results	In-situ neutron at 700 °C	184.3	122.5	45.9	30.9	107.9	39.3	143.1	0.376
	In-situ neutron at 900 °C	134.9	76.8	46.7	29.1	102.3	38.7	96.1	0.325
	RUS at RT	197.9	109.5	44.2	44.2	119.9	44.2	139.0	0.356
Theore-	First- principles calculation at -273 °C	211.8	131.2	31.6	43.3	97.3	34.8	158.1	0.397
tical Calcula- tion Results	First- principles calculation at RT	190.2	111.6	33.5	39.3	98.6	35.7	137.8	0.381
Results	Machine learning at RT	-	-	-	-	-	36.6	146.3	-

Table 1. Experimentally- and theoretically-obtained single-crystal and macroscopic-elastic moduli of the NbTaTiV alloy at elevated temperatures. The single-crystal elastic constants, C_{11} , C_{12} , and C_{44} , macroscopic elastic (E_M), shear (G_M), and bulk (K_M) moduli, and Poisson' ratio (v) at RT, 500 °C, 700 °C, and 900 °C are obtained from the diffraction elastic moduli, using the Kroner model, resonant ultrasound spectroscopy (RT), first-principles calculation (- 273 °C and RT), and machine-learning approach (RT).